Extensional reactivation of the Penninic Frontal Thrust 3 Ma ago as evidenced by U-Pb dating on calcite in fault zone cataclasite.

Antonin Bilau[a,b], Yann Rolland[a,b], Stéphane Schwartz[b], Nicolas Godeau[c], Abel Guihou[c], Pierre Deschamps[c], Benjamin Brigaud[d], Aurélie Noret[d], Thierry Dumont[b], and Cécile Gautheron[d].

[a]EDYTEM, Université Savoie Mont Blanc, CNRS, UMR 5204, Le Bourget du Lac, France.

[b]ISTerre, Université Grenoble Alpes, Univ. Savoie Mont Blanc, CNRS, IRD, IFSTTAR, 38000 Grenoble, France.

[c]Aix-Marseille Université, CNRS, IRD, INRAE, Collège de France, CEREGE, Aix en Provence, France.

[d]GEOPS, CNRS, Université Paris-Saclay, 91405 Orsay, France.

Correspondence: Antonin Bilau (antonin.bilau@univ-smb.fr) and Yann Rolland (Yann.Rolland@univ-smb.fr).

Abstract

In the Western Alps, the Penninic Frontal Thrust (PFT) is the main crustal-scale tectonic structure of the belt. This thrust transported the high-pressure metamorphosed internal units over the un-metamorphosed European margin during the Oligocene (34-29 Ma). Following the propagation of the compression toward the European foreland, the PFT was later reactivated as an extensional detachment associated with the development of the High-Durance extensional fault system (HDFS). This inversion of tectonic displacement along a major tectonic structure has been widely emphasized as an example of extensional collapse of a thickened collisional orogen. However, the inception age of the extensional inversion remains unconstrained. Here, for the first time, we provide chronological constraints on the extensional motion of an exhumed zone of the PFT by applying U-Pb dating on secondary calcites from a fault zone cataclasite. The calcite cement/veins of the cataclasite, formed after the main fault slip event, at 3.6±0.4-3.4±0.6 Ma. Cross-cutting calcite veins featuring the last fault activity are dated at 2.6±0.3-2.3±0.3 Ma. $\delta^{13}C$ and $\delta^{18}O$ fluid signatures derived from these secondary calcites suggest fluid percolation from deep-seated reservoir at the scale of the Western Alps. Our data evidence that the PFT extensional reactivation initiated at least ~3.5 Ma ago with a reactivation phase at ~2.5 Ma. This reactivation may result from the westward propagation of the compressional deformation toward the External Alps, combined to the exhumation of External Crystalline Massifs. In this context, the exhumation of the dated normal faults is linked to the eastward translation of the HDFS seismogenic zone in agreement with the present day seismic activity.

1. Introduction

Dating of major tectonic inversions in orogens is generally achieved by indirect and relative dating, but rarely by the direct dating of fault-related minerals using absolute geochronometers. For instance, tectonic cycles are defined worldwide by the sediment unconformities or by exhumation ages through thermochronological investigation. However, the recent progress in U-Pb dating of carbonate using high-resolution Laser Ablation analyses (Roberts et al., 2020) allows us to directly date minerals formed during fault activity and thus to establish the age of tectonic phases by absolute radiometric dates (Ring and Gerdes, 2016; Goodfellow et al., 2017; Beaudoin et al., 2018;). This method is especially well suited to disentangle the successive tectonic motions along a given tectonic structure. U-Pb dating can be coupled to stable isotopic analysis to infer the nature of fluids through time, which may give insights of the scale of fluid circulations and thus the scale of the active tectonic structure and changes in the stress regime (e.g., Beaudoin et al., 2015; Rossi and Rolland, 2014). In the Western Alps, the Penninic Frontal Thrust or PFT represents a major thrust structure at lithospheric scale (e.g., Tardy et al., 1990; Mugnier et al., 1993; Zhao et al., 2015) that accommodated the main collisional phase during the Paleogene-Neogene (e.g., Ceriani et al., 2001; 2004). Later on, this thrust was reactivated as a normal fault, and the extensional deformation is still ongoing (Sue and Tricart, 1999; Tricart et al., 2006; Sue et al., 2007). This transition from compression to extension in a collisional chain has been diversely interpreted to reflect slab breakoff, crustal overcompensation or post-glacial and erosion-induced isostatic rebound (e.g., Champagnac et al., 2007; Sternai et al., 2019). However, until now, no direct dating of the tectonic shift from compression to extension on the PFT has been obtained, which leads to many possible geodynamic scenari. At the present day, a large range of ages for this transition has been hypothesized from ~12 to 5 Ma (Tricart et al., 2006), to only few ten's ka (Larroque et al., 2009) which shows the lack of direct dating of brittle deformation (Bertrand and Sue, 2017). In this study, we applied the Laser Ablation U-Pb dating method on secondary calcites from a cataclasite fault zone that testify of the extensional deformation of an exhumed paleo-normal fault during the PFT inversion.

The purpose of this study is (1) to provide absolute chronological constraints on the structural inversion of the PFT, and (2) give insights into the scale and nature of fluid circulations along this major fault using stable isotope analysis of carbon and oxygen.

2. Geological setting

The western Alpine collisional belt results from the convergence and collision of the European and Apulian plates, which culminated with top-to-the west displacement on the PFT acting as the major Alpine tectonic structure in the Late Eocene to Oligocene times (e.g., Dumont et al., 2012; Bellahsen et al., 2014). This lithospheric-scale structure accommodated westward thrusting of highly

metamorphosed "Internal zone" units over slightly metamorphosed "External zone" units (Fig. 1, Schmid and Kissling 2000; Lardeaux et al., 2006; Simon-Labric et al., 2009; Malusà et al., 2017). The External zone is composed of the European non-metamorphosed Mesozoic and Paleozoic sedimentary cover and its Paleozoic basement corresponding to the External Crystalline Massifs.
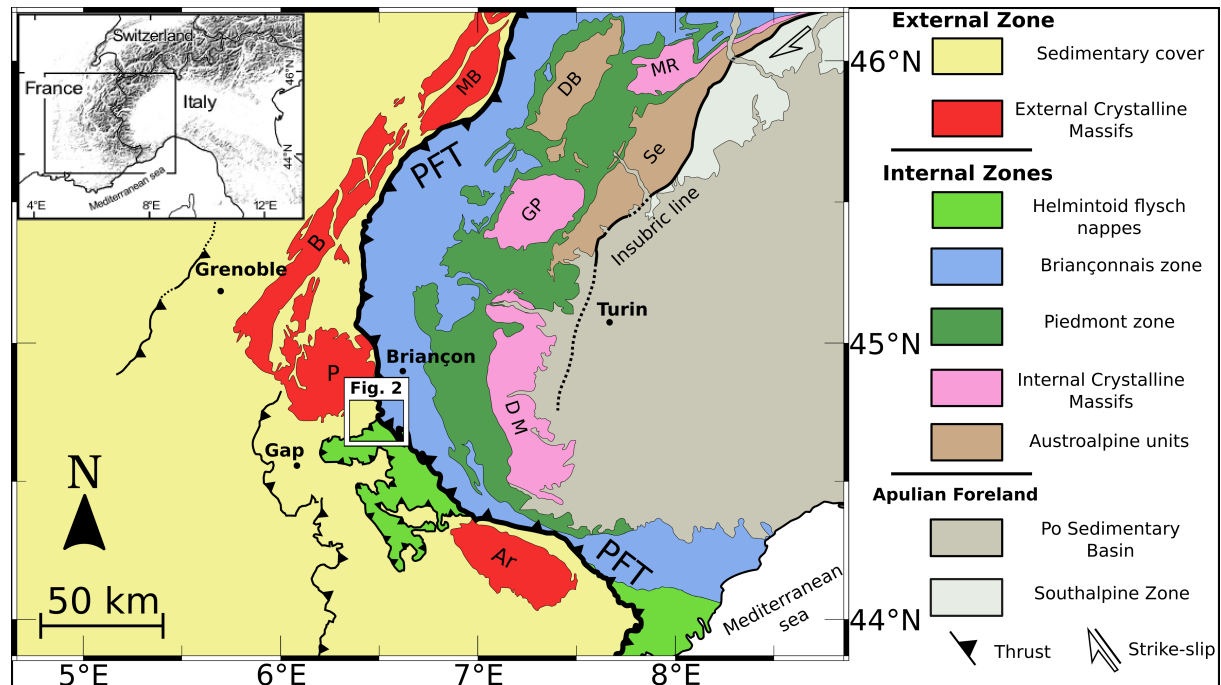
Fig. 1. *Geological map of Western Alps showing the location of the study area. External Crystalline Massifs: Ar, Argentera; B, Belledonne; MB, Mont Blanc; P, Pelvoux. Internal Crystalline Massifs: DM, Dora-Maira; GP, Grand Paradis; MR, Mont Rose. PFT: Penninic Frontal Thrust. Insert modified from Schwartz et al. (2017).*

The Internal zone corresponds to a high-pressure metamorphic wedge formed by the stacking of the paleo-distal European margin of the Briançonnais zone, comprising the Internal Crystalline Massifs and their sedimentary cover, with the oceanic-derived units of the Piedmont zone. These units were incorporated and juxtaposed in the subduction accretionary prism since the Early Late Cretaceous until the Late Eocene (e.g., Agard et al., 2002; Schwartz et al., 2007). The timing of subduction and collision is well constrained by numerous dates on metamorphic minerals (e.g., Duchêne et al., 1997; Rubatto and Hermann, 2001; Lanari et al., 2012, 2014). Eclogite facies recrystallization records subduction of the distal European margin at 32.8 ± 1.2 Ma in the Dora Maira massif, which was later transported as a tectonic nappe during the collision (Duchêne et al., 1997). PFT activation and underthrusting of External Crystalline Massifs are indicators of the transition from subduction to continental collision in the Internal zones, between 44 and 36 Ma (e.g., Beltrando et al., 2009). This transition is marked by shear zone development at greenschist facies conditions and recrystallization during burial of the Alpine External zone in the PFT footwall compartment (Rossi et al., 2005; Sanchez et al., 2011; Bellahsen et al., 2014). The early ductile PFT activity is dated at 34-29 Ma by

⁴⁰Ar/³⁹Ar dating of syn-kinematic phengite from shear zones in the Pelvoux and Mont Blanc External Crystalline Massifs (Seward and Mancktelow, 1994; Rolland et al., 2008; Simon-Labric et al., 2009; Bellanger et al., 2014; Bertrand and Sue, 2017) and by U-Pb on allanite (Cenki-Tok et al., 2014). The age of the PFT hanging wall tectonic motion and joint erosion is highlighted by the exhumation of the Briançonnais units constrained by apatite fission tracks (AFT) at 26-24 Ma (Tricart et al., 1984, 2001, 2007; Ceriani and Schmid, 2004). However, the PFT reactivation as a normal fault remains unconstrained. The onset of PFT extensional activity has been proposed to the Late Miocene (~12 to 5 Ma), based on indirect AFT ages in the Pelvoux External Crystalline Massif (Tricart et al., 2001, 2007), that record a cooling episode related to relief creation and erosion. The current seismicity (e.g., Rothé, 1941; Sue et al., 1999, 2007) and observed GPS motions (Walpersdorf et al., 2018; Mathey et al., 2020), all along the so-called High-Durance Fault System (HDFS) highlight the fact that extensional and minor strike-slip deformations along the PFT are still ongoing. This seismicity mostly occurs at shallow depths, less than 10 km, and mainly at 3 to 8 km, where the HDFS is structurally connected to the PFT (Sue and Tricart 2003, Thouvenot and Fréchet, 2006; Sue et al., 2007).
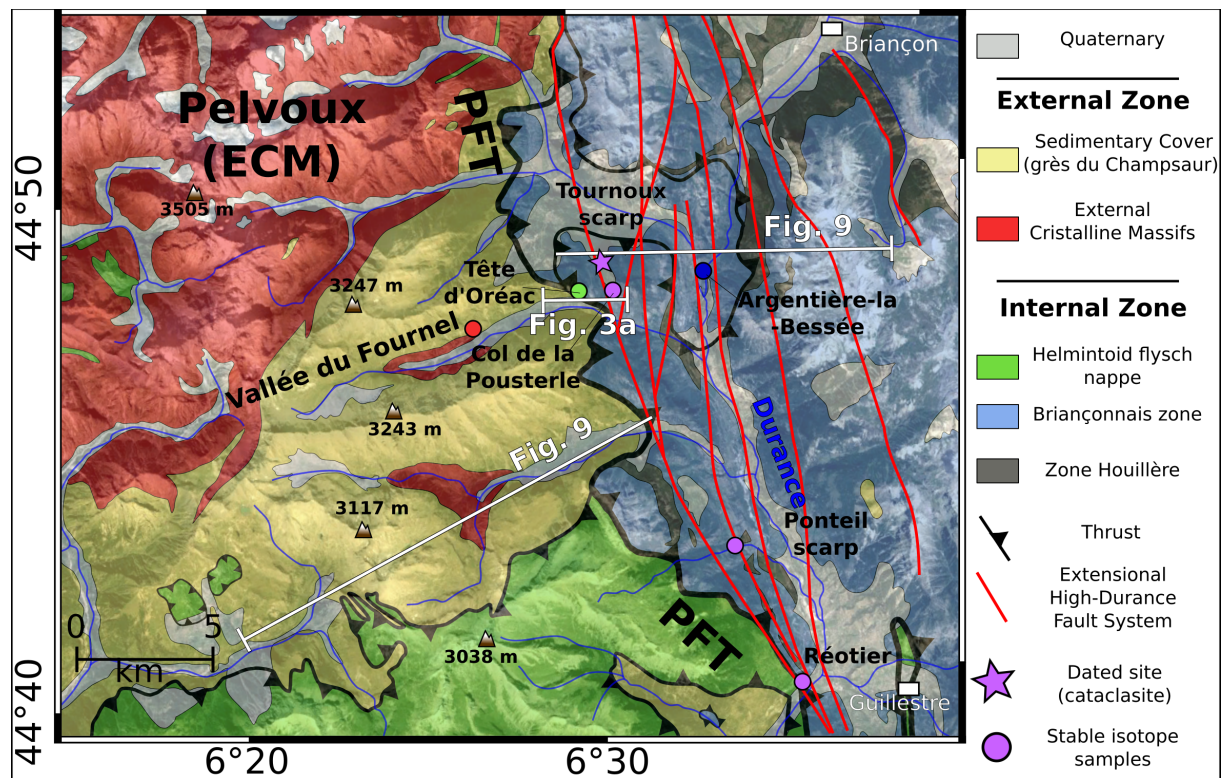
Fig. 2. *Study area of the Penninic Frontal Thrust, east of the Pelvoux External Crystalline Massif (ECM). High-Durance Fault System is represented in red from Tricart et al. (2001) and Sue et al. (2007). Location of sampled sites is indicated. The location of the extensional fault dated by U-Pb on calcite (samples FP18-2 and FP18-3) is marked by a star. Colour of site circle refers to the host rock age: red, Eocene sandstone flysch (grès du Champsaur); green, Cretaceous carbonates; blue, Jurassic carbonates; purple, Triassic carbonates. Sample descriptions are shown on Suppl. Mat. 1. © Google Earth for background relief map.*

The study area is focused on a portion of the PFT located in the southeast of the Pelvoux External Crystalline Massif in the Western Alps (France) (Figs. 1-2). Here, the PFT rests on Late Eocene (Priabonian) autochtonous nummulitic flysch so-called the "Champsaur sandstone" (Fig. 2), which lies unconformably on the Pelvoux crystalline basement. In the southern part, the PFT lies on the Cretaceous Helmintoid flysch nappes, Fig. 2. These two flysch units are intensely deformed by top-to-the-west PFT compressional deformation. The PFT hanging wall corresponds to the Briançonnais zone composed of Mesozoic and Paleozoic sedimentary units, which underwent high pressure metamorphism (Lanari et al., 2012; 2014). The Briançonnais zone is composed of the Briançonnais Zone Houillère, which consists of Carboniferous sediments overlying a crystalline basement, stratigraphically overlain by Middle Triassic to Cretaceous sediments (limestones and calcschists). The PFT structure is well shown in the Tête d'Oréac section of the Fournel Valley transect (Fig. 3, Sue and Tricart, 1999). Here, normal faults cross-cut the Briançonnais series and branch down on the PFT, which was reactivated as a detachment (Tricart et al., 2001).
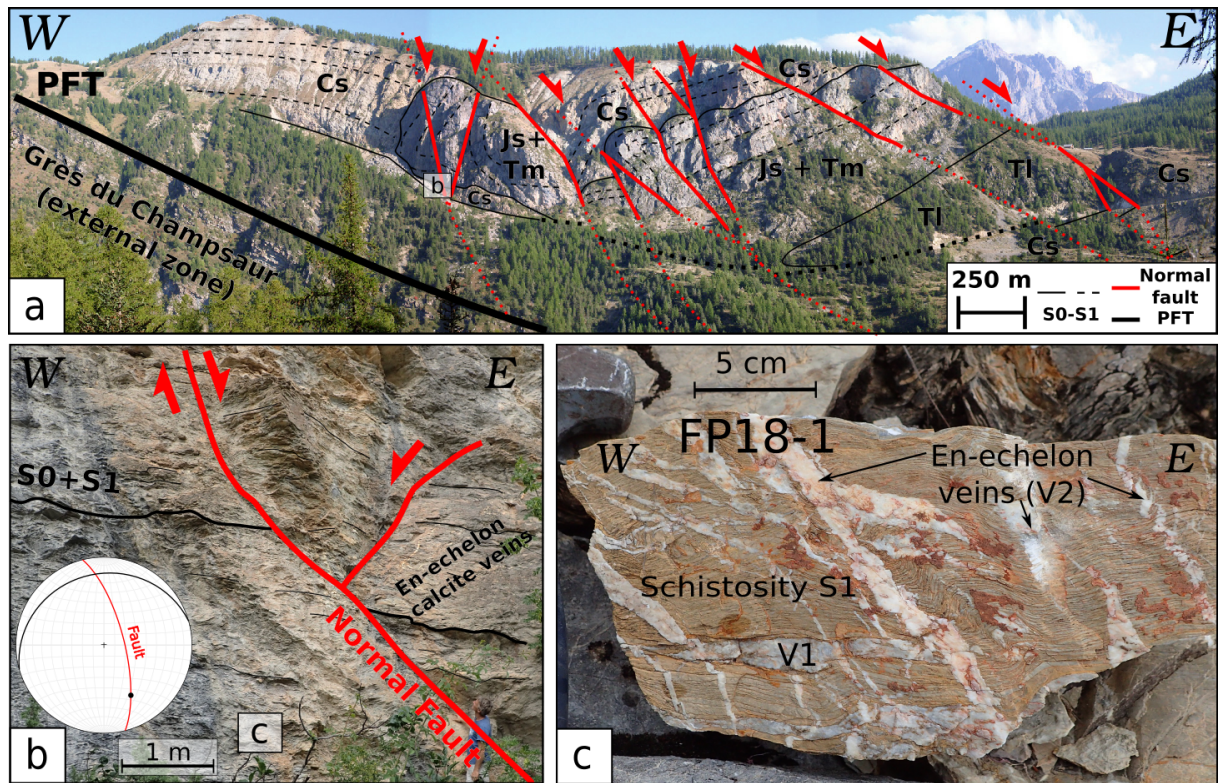
Fig. 3. a: *General view and geological interpretation of the Fournel Valley southern slope with the studied site of the Tête d'Oréac.* **b:** *Outcrop interpretation of the Tête d'Oréac with extensional features in late Cretaceous calcschists in agreement with the High-Durance Fault System and Wulff stereogram, lower hemisphere.* **c:** *Calcschist oriented sample FP18-1 evidencing multiple calcite vein generations. V1 is related to the main compressional phase related to the Tête d'Oréac anticline formation and V2 are related to extensional reactivation of the PFT during onset of the High-Durance Fault System. Cs: Late Cretaceous calcschists; Js+Tm: Middle Triassic to Late Jurassic dolomitic to siliceous limestones; Tl: Lower Triassic sandstones.*

132   The normal faults are tilted by a passive rotation of about 30 degrees towards the west during their
133   exhumation in relation with the activity of the High-Durance Fault System (Sue et al., 2007).

134

135   **3. Sampling strategy and analytical methods**

136   *3.1. Sampling strategy*

137   We collected key samples of each brittle-ductile deformation phase, both in the PFT footwall and
138   hanging wall (Suppl. Mat. 1), to provide a petrographic and stable isotopic dataset which will allow
139   discussing the nature of fluids throughout the PFT activity associated to the late compressional and
140   extensional history. Field analysis is supported by petrographic observations on 28 samples, including
141   8 host rocks, 6 from compressive structures and 14 from extensive structures. Based on this dataset,
142   we selected three fault breccia samples to date the PFT extensional reactivation.

143

144   *3.2. Cathodoluminescence*

145   Cathodoluminescence (CL) analysis provides shades that are mainly representative of oxidation state
146   of trace element and their contents, i.e. Mn^{2+} and Fe^{2+} (Barnaby and Rimstidt, 1989). These differences
147   in calcite chemical composition are an indicator of different mineral precipitations related to slight
148   variations in fluid composition (Goodfellow et al., 2017). CL can also highlight crystal growth patterns
149   or grain boundary interactions (Beaudoin et al., 2015). Using cross-cutting criteria as well as CL, a
150   relative chronology of the calcite generations and related microstructures has been made. Analyses
151   were performed with a spot camera mounted-Cathodyne device (cold cathode) with the following
152   parameters: vacuum ~50mTorr; voltage 16-18 kv; electron beam ~200 µA. Used description
153   terminology is based on Bons et al. (2012).

154

155   *3.3. O and C stable isotope analysis*

156   Stable isotope measurements were achieved on the different generations of microstructures identified
157   by thin section observations and CL images, at Geosciences Paris Sud (GEOPS) laboratory of the
158   Paris-Saclay University, France. Results are presented in Table 1. The protocol is described in detail by
159   Andrieu et al. (2015). Several milligrams (~1mm^3) of sample for each calcite generation were
160   collected using a Dremel 4000 with a 3.2 mm head. Samples were then dissolved with pure
161   orthophosphoric acid (H_3PO_4): Sample tubes provided with two compartments (one for the sample and
162   one for the acid) were sealed under a pressure of 1.5×10^{-2} mbar. They were immersed in a water bath at
163   25°C before the acid was poured on the sample and let to react for 24 h. Complete reaction is
164   necessary to avoid any artificial isotopic fractionation. The produced CO_2 is collected using an
165   extraction line and a liquid nitrogen trap is used to ensure that only CO_2 is collected. Pure CO_2 is
166   analyzed on a VG Sira 10 dual inlet IRMS (Isotope Ratio Mass Spectrometer). Data validity is

167   supported by concurrent analysis of the international standard IAEA CO-1. $\delta^{13}C$ and $\delta^{18}O$ are

168   expressed in ‰ relative to V-PDB (Vienna Pee Dee Belemnite) by assigning a $\delta^{13}C$ value of +1.95‰

169   and a $\delta^{18}O$ value of −2.20‰ to NBS19, (1).

170 $$\delta^{13}C = \left[\frac{\left(^{13}C/^{12}C\right)_{Sample}}{\left(^{13}C/^{12}C\right)_{Reference}} - 1\right] \times 1000 \quad \textit{(1)}.$$

171   For oxygen isotope measurements, switch from PDB values to SMOW (Standard Mean Oceanic

172   Water) were made using the Kim et al. (2015) equation, (2).

173 $$\delta^{18}O_{SMOW} = 1.03086 \times \delta^{18}O_{PDB} + 30.86 \quad \textit{(2)}.$$

174   The ratio of carbon and oxygen isotopes is related to the parental fluid of calcite and can be used as a

175   fluid tracer. Reproducibility was checked by replicate analysis of in-house standards and was ±0.2‰

176   for oxygen isotopes and ±0.1‰ for carbon isotopes.

177

178   *3.4. U-Pb dating of calcite*

179   In-situ uranium and lead isotope analyses of carbonates were carried out at CEREGE (Centre

180   Européen de Recherche et d'Enseignement des Géosciences de l'Environnement), Aix-en-Provence,

181   France. Results are presented in Suppl. Mat. 2. Data were acquired on 150 µm thick thin sections.

182   Laser ablation analysis was performed with an ESI excimer Laser Ablation system with a 6 inches two

183   volume cell (ESI), coupled to an Element XR SF-ICP-MS (Sector Field Inductively Coupled Mass

184   Spectrometer, Thermo-Scientific). Analyses were done at 10 Hz and 1.1-1.15 J.cm^{-2}. Samples were

185   first screened to check signal intensities and maximise the spread of $^{238}U/^{206}Pb$ ratios (e.g. map of

186   Suppl. Mat. 3) to obtain the highest U-Pb variability. A typical analysis consists of 3 seconds of pre-

187   ablation to clean the sample surface, followed by 20 seconds of gas blank and ~20 seconds of

188   measurement on a static circle spot of 150 µm diameter (approximately 8-9 acquisition cycles per

189   second). These parameters lead to approximately ~20-25 µm depth hole (~1 µm/s) on a carbonate

190   material. Ablated particles are carried out of the cell with a He gas flux of 1300 ml/min and then

191   mixed with Ar sample gas (typically 0.8-0.9 l/min). Unknown samples were corrected by standard

192   bracketing with synthetic NIST-614 glass for instrumental drift and lead isotope composition

193   (Woodhead et al. 2001) and a natural calcite spar WC-1 of 254.4 ± 6.4 Ma (Roberts et al., 2020) for

194   inter-elemental fractionation effect, every 20 measurements. No downhole correction was applied

195   since no natural calcite standard with homogeneous U-Pb ratio allows such correction. However, the

196   large aspect ratio used in this set up is supposed to limit this effect. Unknown sample were first

197   processed with the Iolite software (Paton et al., 2011) for baseline correction. Raw ratios were then

198   reduced for instrumental drift, lead isotope composition and inter-elemental fractionation using an in-

199   house excel spreadsheet macro designed for carbonate samples. Ages are obtained using IsoplotR

200   software and plotted in a Tera-Wasserburg diagram using model (1) age (Vermeesch, 2018). An

 additional error propagation of 2.51% in quadratic addition on the final age, tied to the WC-1 standard,

202 is expressed in brackets in the Tera-Wasserburg plot.

203

4. Results

4.1. Deformation phases and miscrostructures

4.1.1. Brittle-ductile deformation features

During the westward thrus motion, the Tête d'Oréac cross-section passes through the PFT (Fig. 3) and

preserves a succession of units that were stacked on each other during to the west thrust motion of the

PFT. The main schistosity (S1) is parallel to the initial bedding (S0) in Cretaceous calcschists. S0-S1 is

sub-horizontal and penetrative throughout the studied area. At the outcrop scale, S1 is clearly visible

and shows dissolution surface with the development of stylolithic joints (Fig. 4).
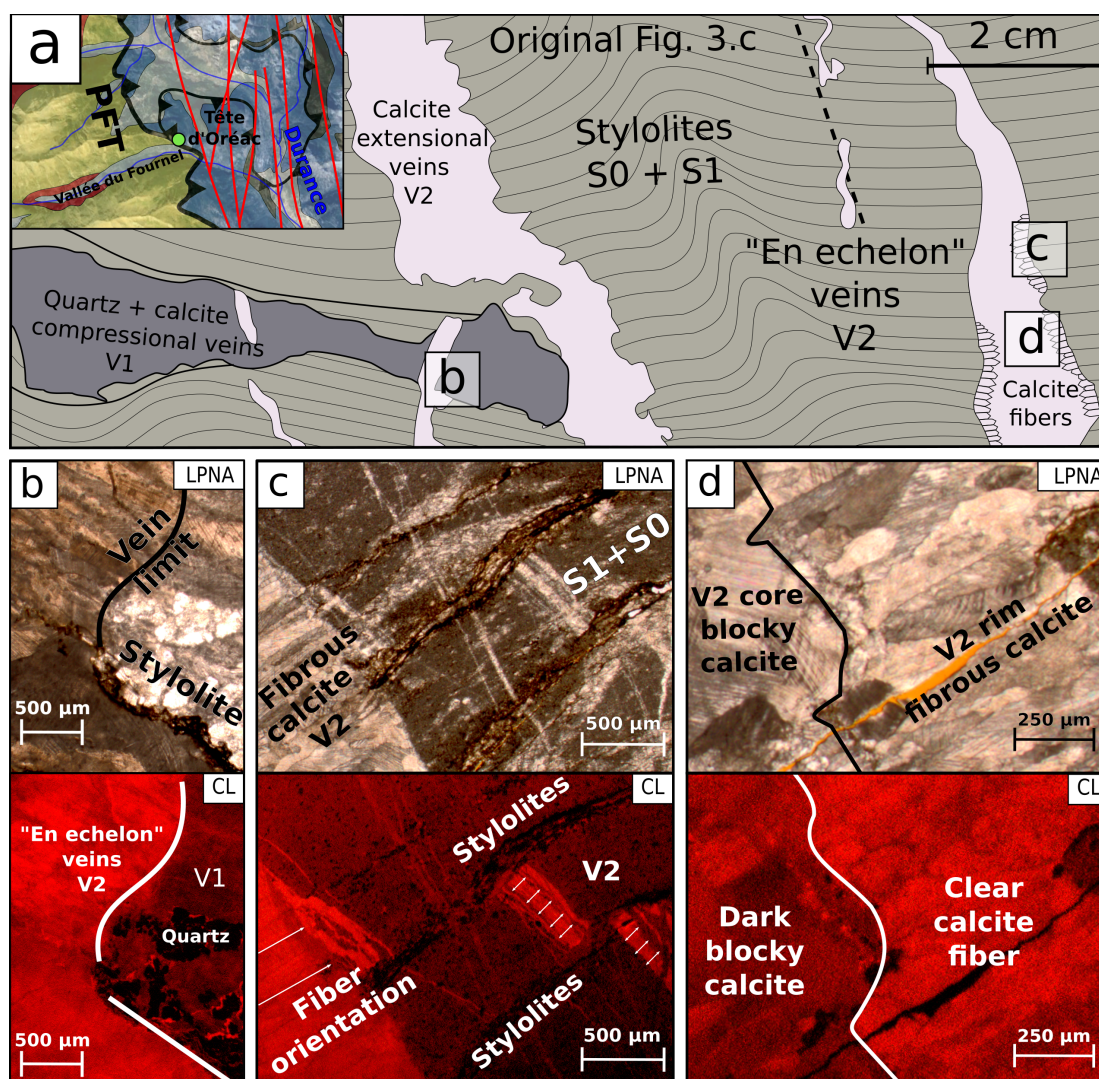
Fig. 4. a: *General sketch of sample FP18-1 evidencing cross-cutting relationships for two main vein generations fig. 3.c.* **b-d:** *Microscope and cathodoluminescence pictures showing the different vein calcite generations.*

214 Quartz anisotropy is observable in LPA which indicate an important deformation syn-post V1. This
215 correlate a strong transposition of structures during PFT compressive motion or opened initially near
216 parallel to S1 either way a ductile deformation is recorded. These early compressional features are
217 cross-cut by numerous steeply dipping eastward normal faults linked to the extensional reactivation of
218 PFT. Early stages of extension are featured by centimetre scale "en-echelon" veins (V2) indicative of
219 an early brittle-ductile extensional deformation followed by dissolution on the horizontal composite
220 (S0-S1) cleavage. Larger V2 veins, expressed at centimetre scale, cross-cut the cleavage and show
221 elongated calcite fibres of ~1000 µm at the vein walls (Fig. 4). Similar shades for early V2 and fibrous
222 V2 are observed in CL. At vein cores, the fibrous calcite is then replaced by a blocky calcite that is
223 less luminescent in CL.
224
225 4.1.2. Brittle deformation features
226 The internal structure of one major extensional fault is investigated in the Tournoux scarp (Fig. 5). The
227 fault zone is highlighted by a metre-scale cataclasite fault gouge with variable amounts of
228 deformations. The top-to-the East (N90°E) normal sense of shear is represented by sigmoids and
229 down-dip slickenside. At thin-section scale, for sample FP18-2, the cataclasite is composed of
230 centimetre-scale host rock clasts with very small (<20 µm) limestone grains. Two types of calcite
231 fillings have been identified. The first one contains organic matter has a « dusty appearance » with
232 bright shades in CL (Fig. 5C). The second one shows large and clear crystals that grew in the cracks
233 and porosity, showing sector zoning patterns highlighted in CL and Laser Ablation-Inductively
234 Coupled Plasma-Mass Spectrometry (LA-ICP-MS) maps (Fig. 5D; Suppl. Mat. 3). ~700 µm large
235 hexagonal, clear and organic matter free, calcite crystals have been selected for U-Pb dating.
236 These calcite crystals represent the latest pervasive fluid circulation episode through the porosity and
237 provide a minimum age for the cataclasite. In sample FP18-3, the matrix is cross-cut by calcite veins
238 with variable diameters (300-1300 µm) and is free of any further deformation. On the basis of their
239 homogeneity and their youngest relative age relationships, these late calcites have also been targeted
240 for U-Pb calcite dating (see section 4.3). Samples FP19-12A-B (described in supplementary data)
241 were collected in a west-dipping conjugate normal fault and exhibits similar deformation features.
242
243 *Fig. 5. a-b: Outcrop interpretation of the Tournoux scarp showing various degrees of cataclasis in Triassic*
244 *dolomitic limestone with Wulff stereogram lower hemisphere. Squares are sampled area, sample FP18-2 is a*
245 *highly cataclased sample, while sample FP18-3 is less intensely cataclased and is cross-cut by millimeter-scale*
246 *calcite veins. c, d, e: Microscope and cathodoluminescence pictures showing several calcite filling generations.*
247 *« clear calcite » shows zonings and seems to crystallize into a primary porosity left within the cataclasite. The*
248 *clear calcite and veins from the cataclasite are dated using the U-Pb dating on calcite method.*
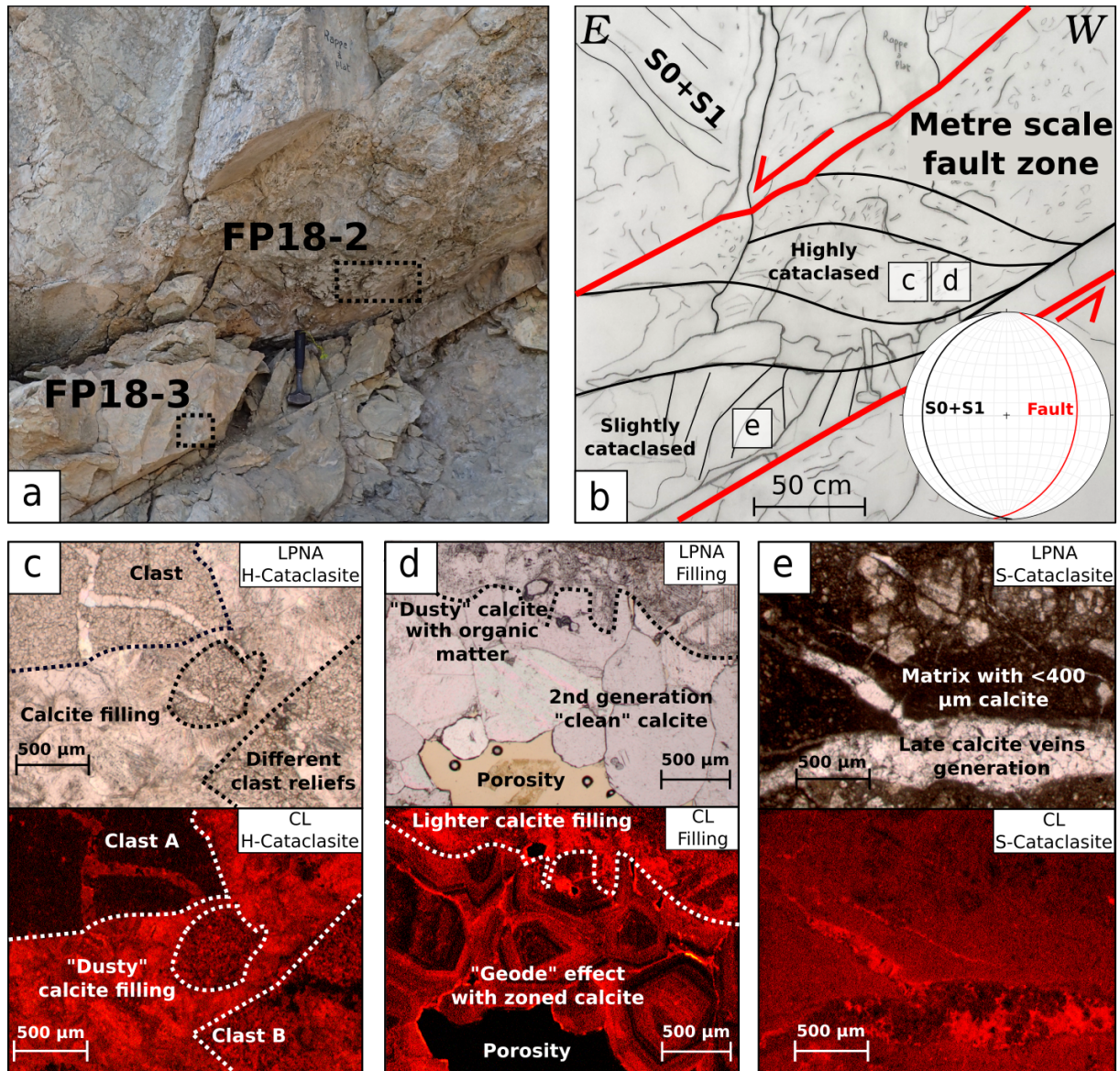
4.2. $\delta^{13}C$ and $\delta^{18}O$ stable isotope results

250

251 Stable isotopes analyses were performed in calcites from various host rocks samples belonging to the

252 different units highlighted in the studied PFT section (Fig. 3) and are supposed to be representative of

253 the different (compressional and extensional) key tectonic phases (Fig. 6).

254 For host rock analysis, upper Cretaceous planktonic calcschists from the Tête d'Oréac show the lowest

255 $\delta^{18}O$ host rock value of 16.8-17.1 ‰ and of $\delta^{13}C$ of 2.1-2.2 ‰. Triassic carbonates show a range

256 between 23.7-26.5 ‰ for $\delta^{18}O$ and between 1.9-2.3 ‰ for $\delta^{13}C$ (with a higher value of 3.4 ‰ for the

257 Ponteil scarp). Upper Jurassic calcshists gave $\delta^{18}O$ ratio of 28.5 ‰ and $\delta^{13}C$ of 1.3 ‰. The western

258 Late Eocene Flysch (Champsaur sandstone) gave lowest $\delta^{13}C$ ratio of -0.3 ‰ and a $\delta^{18}O$ ratio of 21.9

259 ‰. Analysed brittle-ductile veins either related to the compressional or to the onset of the extensional

260 tectonic phases stand very close to their host rocks, near to the meteoric water field defined by Nardini

et al. (2019) (Fig. 6). However, the V2 veins associated to the brittle normal fault development, clearly show lower $\delta^{18}O$ values (<15‰) compared to their host rocks, with a trend towards lower $\delta^{13}C$ values. These isotope signatures are similar to those measured in calcite from veins of the Mont Blanc External Crystalline Massifs (Rossi and Rolland, 2014).
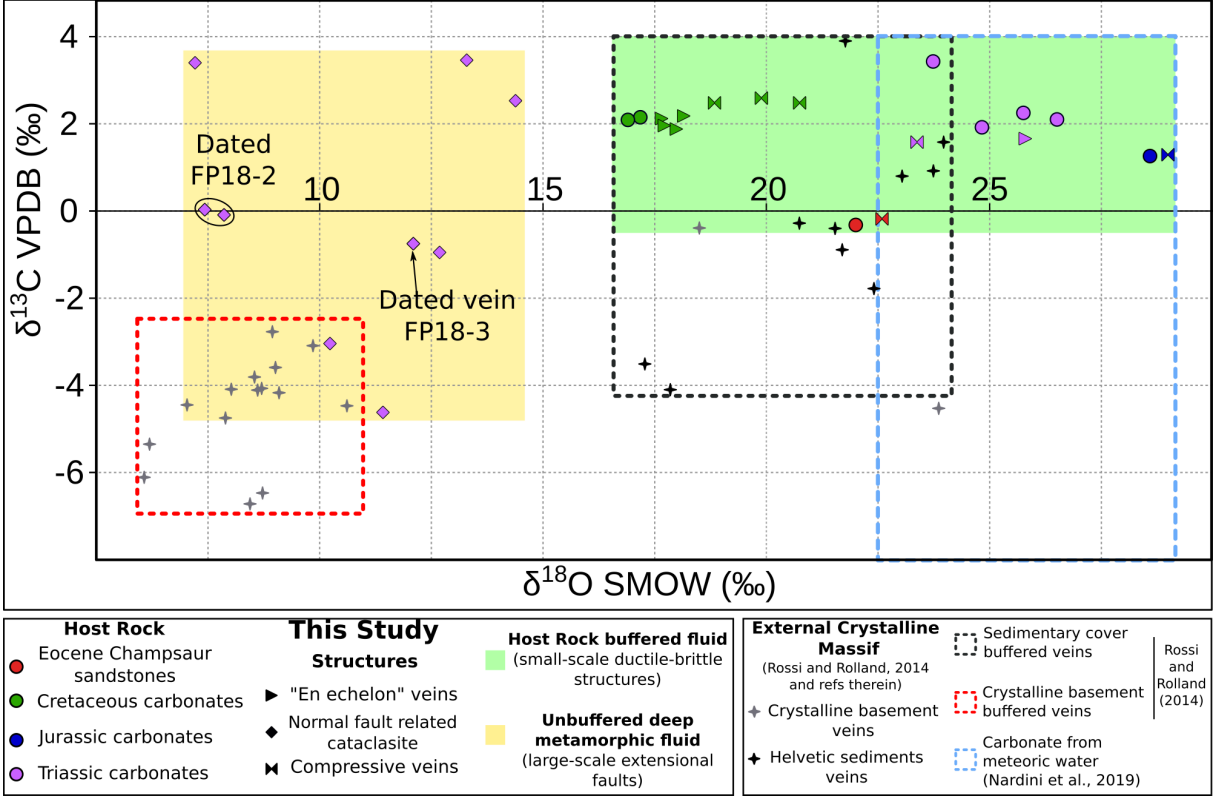
Fig. 6. *Stable isotopic data from samples indicated on Fig. 2. Domains represented by dashed red, black and blue lines are from the literature (Nardini et al., 2019; Rossi and Rolland, 2014 and references therein). The coloured green domain corresponds to veins associated to brittle-ductile structures. These veins show similar isotopic compositions as their host rocks. The orange domain features the signature of cataclased normal fault samples, which show a different isotopic composition as compared to their host rock, and are similar to deep metamorphic fluids (e.g., Crespo-Blanc et al., 1995; Rossi and Rolland, 2014; Rolland and Rossi, 2016).*

4.3. Calcite LA-ICPMS U-Pb dating results

Petrographic analysis has been complemented by screening using LA-ICP-MS on 24 thin-sections from samples of 7 locations around the PFT related to compressive and extensive structures. Among these, 20 screened samples show high common lead contents, and sometimes higher lead to uranium intensity signals. U-Pb dating of such carbonates with high lead concentrations remains highly challenging, especially for very young samples. However, four samples (samples FP18-2, 3 and FP19-12A&B described in section 4.1 and supplementary data) from the Tournoux normal fault site bear sufficient [238]U (~0-8.5 ppm for FP18-3A&B and ~0-4.5 ppm for FP18-2B and FP19-12A&B), and [206]Pb, [207]Pb (~0-1.9 ppm for FP18-3A&B and ~0-13.1 ppm for FP18-2B and FP19-12A&B).
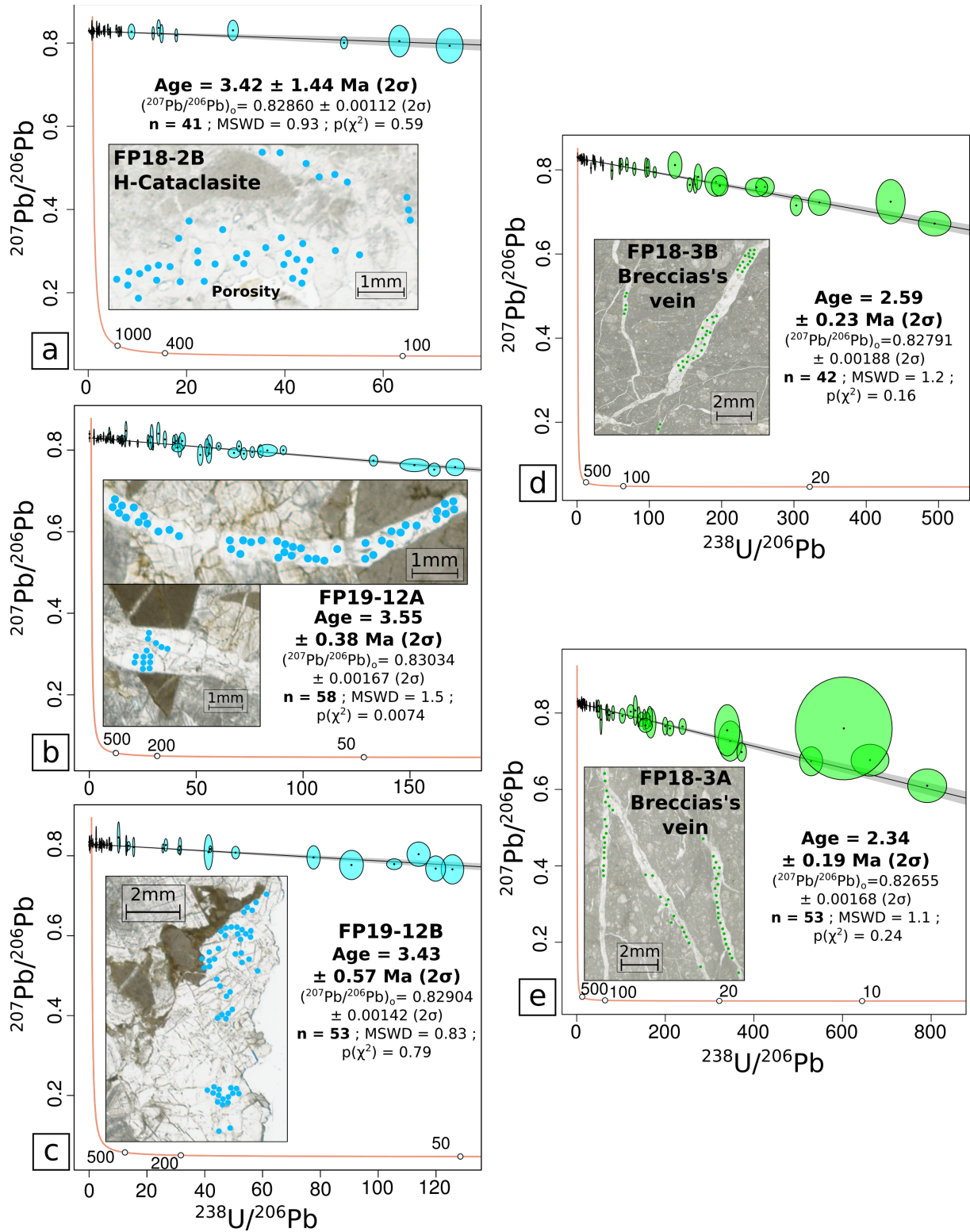
Fig. 7. *Tera-Wasserburg concordia plot of (a) Highly cataclased sample FP18-2 calcite filling (b) and (c) sample FP19-12A veins and FP19-12A 'clean calcite' filling (d) and (e) sample FP18-3 veins, and corresponding maps of sampled spots (150 µm). MSWD: Mean Square Weighted Deviation. An additional error propagation tied to WC-1 standard uncertainty is taken into account.*

286 Lead contents are based on NIST614 intensities and uranium contents are based on WC-1 intensities

287 (Jochum et al., 2011; Roberts et al., 2017; Woodhead et al., 2001), giving measurable and significant

288 radiogenic signal. Five ages have been obtained on these four samples (Fig. 7).

289 A first group of ages of ~3.5 Ma is represented by three samples. The cataclasite 'clean calcite' infill

290 (sample FP18-2B; Fig. 5) gives age of 3.42±1.44 Ma (n=41, MSWD=0.93). This quite large

291 uncertainty is due to a relatively moderate U/Pb variability and the resulting low radiogenic signal

292 measurable in this sample. Samples FP19-12A&B give two similar within-error ages for the vein

293 calcite and 'clean calcite' infill, of 3.55±0.38 (n=58, MSWD=1.5) and 3.43±0.57 (n=53,

294 MSWD=0.83), respectively.

295 A second group of ages of ~2.5 Ma is obtained on different cross-cutting veins of the latest generation

296 of sample FP-18-3 (Fig. 5), represented by slightly younger, but distinct out of error margins, ages of

297 2.59±0.23 Ma (n=42, MSWD=1.2; FP-18-3B in Fig. 7b) and 2.34±0.19 Ma (n=53, MSWD=1.1; FP-

298 18-3B in Fig. 7c). The higher spread in U/Pb ratios measured in these two latter ages results in more

299 precise and robust ages. These two age groups obtained on extensional faults connected to the PFT

300 highlight for the first time at least two phases of deformation constrained out of error bars: a first

301 phase of brittle deformation forming the cataclasite at 3.5±0.4 and one or two discrete brittle events at,

302 or comprised within, 2.6±0.2 and 2.3±0.2 Ma. These ages show that the sated conjugated faults have

303 beed active for at least 1 Myr, and are featured by only several datable events, representing co-seismic

304 motions on the faults.

305

306 **5. Discussion**

307 Onset of extensional tectonics in the Alps has remained a topic of debate for the last 20 years. A

308 Miocene age has been proposed for the onset of the extensional activation of the PFT based on AFT

309 datings on both sides of this major fault, i.e. in the Pelvoux External Crystalline Massif and in the

310 Champsaur sandstones to the west and in the Briançonnais zone to the east (Tricart et al., 2001; 2007;

311 Beucher et al., 2012). The Briançonnais zone corresponds to the east hanging wall compartment of the

312 PFT. In this compartment, AFT ages ranging from 30 Ma to 20 Ma are interpreted as the exhumation

313 age of this area related to the compressional activity of the PFT during the Alpine collision, which

314 motion is constrained by direct $^{40}Ar/^{39}Ar$ dating on phengite at 35-25 Ma (Simon-Labric et al., 2009;

315 Bellanger et al., 2015). To the west (footwall of the PFT), the AFT ages range from 13 Ma to 4 Ma in

316 the Pelvoux External Crystalline Massif (Beucher et al., 2012), and from 9 to 4 Ma in the Champsaur

317 sandstones (Tricart et al., 2007), and are interpreted as the extensional reactivation of the PFT by these

318 latter authors. As the AFT dates record an exhumation age associated with cooling below ~100°C

319 (Ault et al., 2019), they may not correspond to an age of PFT activity but rather record an erosion

320 process that is related to both climatic and tectonic processes (e.g., Champagnac et al., 2007). Sternai

321 et al. (2019) suggest that vertical movement in the Western Alps may be mainly ascribed to erosion
322 and deglaciation (Nocquet et al., 2016) and may also include a significant mantle convection
323 component (Salimbeni et al., 2018). However, the External Crystalline Massifs exhumation was also
324 driven by frontal thrusting, activated during middle Miocene at the western front of these massifs
325 (Boutoux et al., 2015) and by strong erosional processes that enhanced exhumation since the Late
326 Miocene (Cederbom et al., 2004). Along the PFT, younger AFT and phengite $^{40}Ar/^{39}Ar$ ages of ~10 Ma
327 were obtained on the Plan de Phasy (Guillestre) metagranite mylonites (Tricart et al., 2007; Lanari et
328 al., 2014). These ages have been interpreted as the result of hydrothermal fluid circulation, which may
329 be linked to tectonic activity of the High-Durance Fault System. However these fluid circulations may
330 be passive through the PFT network and may not correspond to extension onset. Therefore, the age of
331 PFT activity remains unconstrained and requires some direct datings. In the following discussion, we
332 show how absolute U-Pb dating of fracture infill calcite brings quantitative time constraints on PFT
333 fault movement.
334
335 *5.1. Deformation and scale of fluid flow in the brittle-ductile structures*
336 The measured $\delta^{18}O$ and $\delta^{13}C$ isotope ratios of veins from brittle-ductile structures are close or similar
337 to their host rocks, and remain close to the field of carbonates precipitated from meteoric water
338 (section 4.2). Based on several studies in the frontal parts of Alpine orogens (Smeraglia et al., 2020;
339 Nardini et al., 2019), these isotope signatures are thought to be representative of meteoric water inflow
340 from the most superficial domains. Three important parameters are involved to control this surface-
341 derived fluid regime: (i) lack of large-scale structures (ii) pressure-solution microstructures (evidence
342 of local fluid) (iii) presence of a shallow impermeable clay-rich layers which isolate upper crust from
343 more deeply-rooted systems (section 4.1. and Fig. 3). Rossi and Rolland (2014) report similar stable
344 isotope signatures in the Mont Blanc External Crystalline Massif sedimentary cover (Helvetic schists).
345 There, the vein calcites bear similar stable isotope values as the host Helvetic schists, which is in
346 agreement with the fluids to have equilibrated with their host rocks in a closed system with low
347 fluid/rock ratios (Rolland and Rossi, 2016). In our study, observations of veins show that they were
348 closely related to schistosity acting as a stylolithic dissolution surface (section 4.1). This observation is
349 consistent with local fluid interactions and equilibrium with the host rock, resulting from a pressure-
350 dissolution-recrystallization transfer mode (e.g. Passchier and Throw, 2005). Based on this, we suggest
351 that the external fluid signature was buffered by the host rock signature. These fluid compositions
352 show that 'en-echelon' veins are linked to an early deformation, where the porosity was still not
353 connected by the fault network (Fig. 3). In such a system, the veins kept the host rock signature and no
354 crustal-scale fluid flow circulation is evidenced.
355

5.2. Scale of fluid flow in the brittle extensional structures

Major (> metre-scale width) faults are related to shallower, or higher stress contexts (e.g. Passchier and Throw, 2005). The isotopic composition of calcite that crystallised in these brittle extensional faults is significantly different from their host rock (section 4.2; Fig. 6). Indeed, calcites related to these major faults have $\delta^{18}O$ lower than 10 ‰ from their host rock and a $\delta^{13}C$ ranging between -5 to 4 ‰ PDB (while the $\delta^{13}C$ ratio of Trias host rock is of 2 ‰). This signature is similar to that of exogenous metamorphic fluid origin (Crespo-Blanc et al., 1995; Rossi and Rolland, 2014). The observed CL pattern of calcites also argues for variations in the fluid composition, between the different veins and progressively within a given vein. Similar signatures are recorded in the Mont Blanc External Crystalline Massif shear zones and veins in a similar structural context (Rossi et al., 2014). There a similar spread of $\delta^{13}C$-$\delta^{18}O$ values is observed in the marginal part of the crystalline basement, at the contact with the Helvetic schists. This spread is interpreted as a mixing between fluids flowing down through the sedimentary cover and upwards fluids originating from shear zones in the Massif Central (Rolland and Rossi, 2016). The chemical signature of calcite veins in the Massif Central shear zones is correlated to a Mg-K-rich metasomatism, both arguing for CO_2-bearing fluids representative of a deep source, which is rooted in the mantle via vertical shear zones (Rossi et al., 2005). This deeply rooted fluid cell is also suggested by fluids significantly hotter (150-250 °C) than their host-rock at ca. 10 Ma along vertical faults in Belledonne Massif, which are in continuity with the central Mont Blanc Massif shear zones (Janots et al., 2019). Indeed, deep metamorphic fluid circulation is in good agreement with a crustal-scale fluid pathway which is activated during the extensional motion of the PFT, connected to the Rhône-Simplon right-lateral fault (Bergemann et al., 2019; 2020). This crustal-scale network suggests that extensional faults are in-depth connected to the PFT, when it was reactivated as a detachment. Deep connection with the PFT crustal scale structure (e.g. Sue et al., 2003) would allow fluid circulation from interface of European slab with the deep subduction/collisional metamorphosed prism. In our study, the isotopic dataset shows a significant difference between the deep fluids signature recorded by the Mont Blanc veins (Rossi and Rolland, 2014; Rolland and Rossi, 2016) and the compositions of the veins related to brittle-ductile structures (Fig. 6). This variability suggests a mixing process between the local fluids trapped in the early extensional (closed system) and these exogenous fluids from a deep crustal origin.

5.3. Timing of PFT extensional inversion

All ages obtained from the investigated Tournoux normal fault scarp, give direct time constraints on the final stages of extensional slip, and are interpreted as a minimum age for the extensional reactivation of the PFT. The oldest event is the formation of the highly deformed cataclasite calcite filling/veins ~3.5 Ma (3.4±1.5 Ma, 3.6±0.4 and 3.4±0.6). This calcitic cementation occurred directly

after the main cataclastic deformation event and before the late cross-cutting veins. Latter cross-cutting veins gave the same ~2.5 Ma age, with two within-error dates of 2.6±0.3 and 2.3±0.3 Ma. The ~3.5 Ma and ~2.5 Ma do not represent the same slip event on the fault. It is noteworthy that all these ages are calculated assuming secular equilibrium in the U-series decay chain. As fluids are generally characterized by an excess in ^{234}U with respect to ^{238}U, resulting in an excess of radiogenic ^{206}Pb, the calculated ages should be considered as maximum ages (see for example Walker et al., 2006). The magnitude of the offset ages due to initial ^{234}U/^{238}U disequilibrium can be significant and the true age could be younger by several hundreds of thousands of years. In the present case, it was not possible to carry out classical isotopic analyses of uranium by isotopic dilution to measure any detectable residual ^{234}U/^{238}U disequilibrium because of the size of the carbonate phases. It could be hazardous to speculate on the initial ^{234}U/^{238}U disequilibria of the fluids, but the quite high uranium concentrations (up to the ppm level) observed in analysed minerals of samples FP-18-2 & 3 (Fig. 7) are likely indicative of an oxidizing environment and thus of a moderate initial ^{234}U excess (Walker et al., 2006). To assess the impact of this excess on the final age, we have tested various initial ^{234}U/^{238}U activity ratios ranging between 1 to 2 as illustrated in Figure 8. For an initial (^{234}U/^{238}U) activity ratio of 2, the true age is lower by about ~370 ka. The obtained ages assuming an initial (^{234}U/^{238}U) ratio of 1 are thus regarded as maximum ages.

As they remain undeformed, the latter veins are considered as the youngest tectonic slip along the fault. Furthermore, the geometry of the Tournoux normal fault reguarding the PFT position indicates that this normal fault was connected to the PFT, which acted as a detachment Zone (Fig. 9). Thus, it may represent the paleo-HDFS seismogenic zone, which was later exhumed in the footwall part of the active extensional fault. Main activity of this paleo-fault can be bracketed between 3.4-2.2 Ma based on the above results.
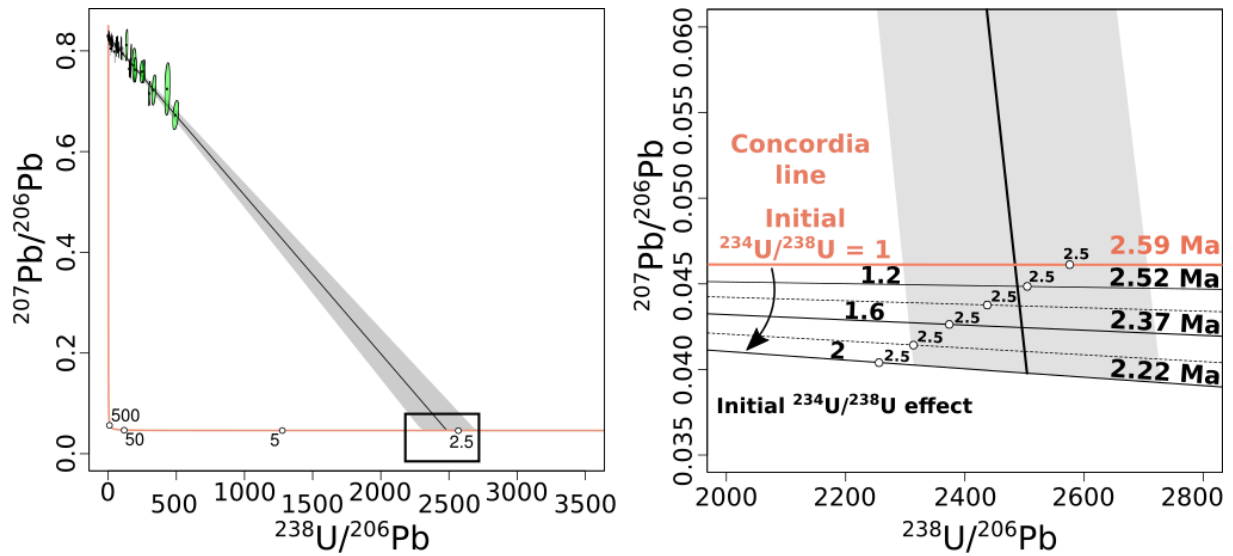
Fig. 8. *Impact of the initial ^{234}U excess on the final age estimation. Several initial $^{234}U/^{238}U$ activity ratios have been tested ranging between 1 to 2. This spread in initial $^{234}U/^{238}U$ leads to an age difference of 0.37 Ma. The obtained U/Pb age of 2.59 Ma, assuming equality of ^{234}U and ^{238}U contents is thus a maximum age.*

5.4. Evolution of PFT through time

The structural and dating results presented in this paper, combined with the literature on PFT footwall and hanging wall exhumation lead to the following reconstitution of its evolution (Fig. 9).

The investigated PFT paleoseismic zone is located 3 to 10 km west of the active HDFS seismogenic zone. Nowadays, the extensional deformation is mainly localised on one active fault and mostly occurs mostly at 3 to 8 km depth (Sue et al., 2007; Mathey et al., 2020). This study gives insights into the uplift rate and lateral displacement of the High-Durance Fault System footwall and hanging wall since the passage of the investigated paleo-PFT through the upper boundary of the seismogenic crust some 2-3.5 Ma ago. Since then, the PFT hanging wall, represented by the active extensional deformation front of the HDFS was significantly shifted eastward, while its footwall was uplifted up to 3 km (Fig. 9). This leads to a mean vertical tectonic motion on the order of > 1 mm.yr^{-1} for the footwall compartment of PFT on this period of time. This rate is consistent with the vertical GPS rates measured for the Pelvoux External Crystalline Massif (Nocquet et al., 2016; Sternai et al., 2019).
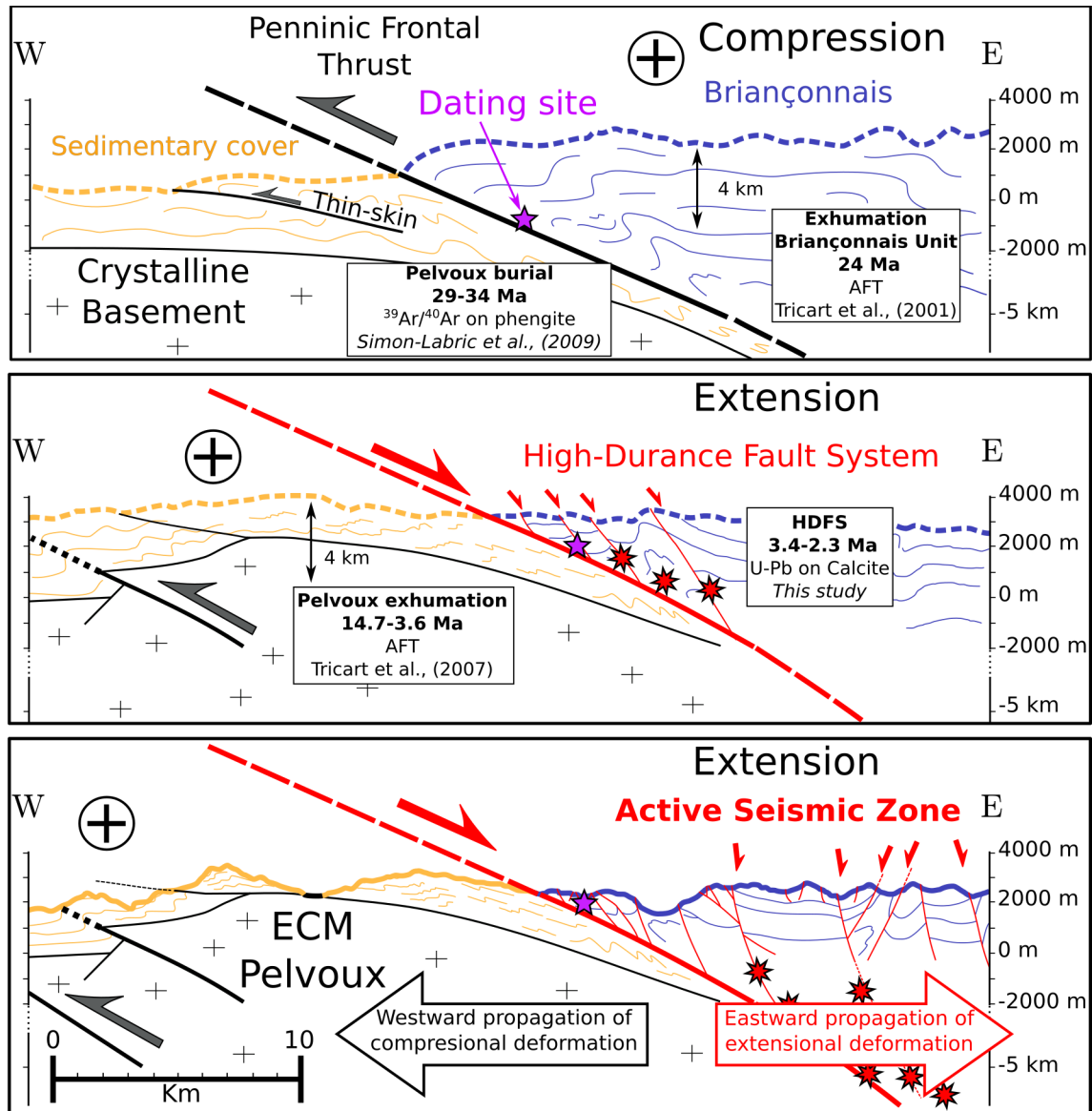
Fig. 9. *Evolutionary geological cross-section sketch of PFT (modified from Tricart et al., 2006).* **a,** *Compressional activation of the PFT resulting in joint External Crystalline Massifs burial and Briançonnais exhumation during the Oligocene.* **b,** *Extensional reactivation of the PFT and setting up of the High-Durance Fault System during the Pliocene as evidenced in this study. At this point the dated extensional fault passes through the upper boundary of the seismic zone at ca. 2-3 Ma.* **c,** *At present-day, compressional deformation has migrated westward (frontal part of External Crystalline Massifs, since c. 15 Ma) and extensional seismic activity of the High-Durance Fault System is recorded at shallow depth 3-10 km east of the studied paleoseismic zone.*

Our data support the hypothesis that the present HDFS is the result of eastward shifting of extensional deformation, accommodated by successive jumps on several faults. Faults were likely active on a scale of ≥1 Myr before becoming inactive. Calcite U-Pb ages obtained on the Tournoux scarp constrain co-seismic motion on two conjugate faults. The two age groups obtained on these extensional faults connected to the PFT highlight at least two phases of deformation, at 3.5±0.4 Ma and one or two

445 discrete brittle events at, or comprised within, 2.6±0.2 and 2.3±0.2 Ma, which gives insights into the

446 long-term activity of the of at least 1 Myr, but with only several datable events, which argues for an

447 apparent contradiction. Indeed, co-seismic displacement on the fault suggest a significant magnitude

448 for the related earthquake (Wells and Coppersmith, 1994), which is apparently incompatible with the

449 very few datable motions. This gives some weight to a deformation regime which may alternate phase

450 of creeping on the fault plane, without any brittle deformation, with very rare phases of brittle

451 deformation.

452 The vertical uplift and exhumation of the Pelvoux External Massif since 3.5 Ma may thus mainly

453 result from the cumulated fault motion on these several fault segments. These data are thus in

454 agreement with a significant tectonic component in the measured uplift signal of External Crystalline

455 Massifs, which is in agreement with a clear difference in uplift rates measured between ECMs and

456 Internal Alps (Nocquet et al., 2016; Sternai et al., 2019).

457 We support the hypothesis that the HDFS is the result of the eastward extensional deformation shift

458 and the successive formation of younger faults normal fault participated at the exhumation of the

459 directly to the west block.

460

461 **6. Conclusion**

462 Significant constraints on the evolution of fault systems can be acquired by coupling stable isotopic

463 analysis and U-Pb dating on calcite. These methods have been successfully applied to unravel the

464 tectonic reactivation of the PFT for the first time. Five U-Pb ages on calcite have been obtained on

465 extensional fault structures connected to the PFT, gave two distinct group of ages of 3.5±0.5 Ma for

466 the main deformation phase represented by the cataclasite calcite cement, cross-cut by later discrete

467 phases represented by mm-large veins dated from 2.6±0.3 to 2.3±0.3 Ma. The 3.5 Ma age represents a

468 minimum age for the onset of extensional brittle reactivation of the PFT. Earliest extensional ductile-

469 brittle structures cannot be dated due to low uranium contents and low U/Pb ratios. Associated to those

470 two (ductile and brittle) deformation stages, stable isotopic ratios of carbon ($\delta^{13}C$) and oxygen ($\delta^{18}O$)

471 of calcite samples collected within the kilometre-scale extensional faults show an evolution from a

472 closed to an open fluid system. The isotopic signature of fluids related to the brittle deformation stage

473 corresponds an open system due to the activation of a crustal-scale fluid circulation cell when the

474 HDFS developed in connection with the deeper PFT deeper structure. The fluids associated to this

475 open system show a deep crustal/mantle signature similar to that measured along the PFT across the

476 Alpine arc. This deeply rooted upward fluid circulation occurred when extensional fault activity was

477 connected to the PFT reactivated as a detachment, which suggests a crustal-scale extensional

478 reactivation at this stage. These constraints on PFT fluid regime are the first direct evidence for a

479 transition towards a crustal-scale fluid regime at the onset of brittle extensional reactivation in the

Alps. The direct ages of PFT motion give insights into the long-term incremental displacement of the HDFS footwall, and Pelvoux Massif exhumation, which corresponds to its passage through the upper part of the seismogenic zone, at a mean rate of > 1 mm.yr^{-1} in the last 3 Ma.

Acknowledgements

This work forms part of first author's Ph.D. funded by the BRGM in the frame of the RGF project. The CEREGE group is supported by 2 French "Investissements d'Avenir" fundings: the EQUIPEX-ASTER-CEREGE and the Initiative d'Excellence of Aix-Marseille University - A*Midex, through the DatCarb project. We wish to thank Fayçal Soufi for his help in sample preparation.

Author contributions

AB, YR and SS wrote the manuscript and all authors discussed the results and contributed to the final article. TD supported AB for map creation and cross-sections. YR, SS, TD, CG and AB participated to field trip sampling. AB did the sample petrographic characterization with optical microscope and cathodoluminescence. NG, AG and PD led U-Pb dating with AB. BB and AN supervised AB for stable isotopes analysis, for results interpretation and protocol application respectively.

Supplementary Materials

Suppl. Mat. Table S1. Sample locations and descriptions.

Suppl. Mat. Fig. S1. Tournoux's scarp general view.

Suppl. Mat. Fig. S2. Field photographies FP19-12 site.

Suppl. Mat. Fig. S3. La-ICPMS elemental maps, FP18-2B.

Suppl. Mat. Fig. S4. FP19-12B thin section with map localisation.

Suppl. Mat. Fig. S5. La-ICPMS elemental map, FP19-12B.

Suppl. Mat. Table S2. U-Pb on calcite La-ICPMS data.

Table 1: Isotopic composition of analysed calcites

	N°Sample	$^{13}\delta$C PDB	$^{18}\delta$O SMOW
Whole Rock	FP18-1A	2,15	17,18
	FP18-1A	2,09	16,90
	FP18-4	1,92	24,83
	FP18-7	2,25	25,76
	FP18-9	-0,32	22,00
	FP18-10	1,26	28,59
	FP18-11	2,1	26,51
	FP18-13	3,43	23,73
Early veins (V1)	FP18-1B	2,59	19,89
	FP18-1C	2,48	20,74
	FP18-1C	2,48	18,84
	FP18-9	-0,18	22,59
	FP18-10	1,29	28,99
	FP18-11	1,58	23,37
En-echelon veins (V2)	FP18-1A	2,12	17,65
	FP18-1A	2,18	18,15
	FP18-1B	1,96	17,71
	FP18-1D	1,88	17,98
	FP18-5	1,66	25,80
Cataclasite infill *(V2)*	FP18-2A	0,03	7,43
	FP18-2B	-0,09	7,86
	FP18-3B	-4,62	11,41
	FP18-3B	-0,75	12,10
	FP18-6	-3,04	10,23
	FP18-6	-0,95	12,68
	FP18-13	3,46	13,29
	FP18-13	2,53	14,38
	FP18-13	3,4	7,21

507 **Table 1.** *Stable isotope data, first bloc for host rock, second bloc compressive veins, third early small scale*

508 *extensional features, fourth main large scale extensional features.*

509

510

Références

Andrieu, S., Brigaud, B., Rabourg, T,. and Noret, A.: The Mid-Cenomanian Event in shallow marine environments: Influence on carbonate producers and depositional sequences (northern Aquitaine Basin, France), Cretaceous Res., 56, 587–607, https://doi.org/10.1016/j.cretres.2015.06.018, 2015.

Ault, A. K., Gautheron, C., and King, G. E.: Innovations in (U–Th)/He, fission track, and trapped charge thermochronometry with applications to earthquakes, weathering, surface-mantle connections, and the growth and decay of mountains, Tectonics, 38(11), 3705-3739, https://doi.org/10.2029/2018TC005312, 2019.

Barnaby, R. J. and Rimstidt, J. D.: Redox conditions of calcite cementation interpreted from Mn and Fe contents of authigenic calcites, Geol. Soc. Am. Bull., 101(6), 795-804, https://doi.org/10.1130/0016-7606(1989)101<0795:RCOCCI>2.3.CO;2, 1989.

Beaudoin, N., Huyghe, D., Bellahsen, N., Lacombe, O., Emmanuel, L., Mouthereau, F., and Ouanhnon, L.: Fluid systems and fracture development during syn-depositional fold growth: An example from the Pico del Aguila anticline, Sierras Exteriores, southern Pyrenees, Spain. J. Struct. Geol., 70, 23–38, https://doi.org/10.1016/j.jsg.2014.11.003, 2015.

Beaudoin, N., Lacombe, O., Roberts, N.M.W., and Koehn, D.: U-Pb dating of calcite veins reveals complex stress evolution and thrust sequence in the Bighorn Basin, Wyoming, USA. Geology, 46, 1015–1018, https://doi.org/10.1130/G45379.1, 2018.

Bellahsen, N., Mouthereau, F., Boutoux, A., Bellanger, M., Lacombe, O., Jolivet, L., and Rolland, Y.: Collision kinematics in the western external Alps, Tectonics, 33(6), 1055-1088, https://doi.org/10.1002/2013TC003453, 2014.

Bellanger, M., Augier, R., Bellahsen, N., Jolivet, L., Monié, P., Baudin, T., and Beyssac, O.: Shortening of the European Dauphinois margin (Oisans Massif, Western Alps): New insights from RSCM maximum temperature estimates and $^{40}Ar/^{39}Ar$ in situ dating, J. Geodyn., 83, 37–64, https://doi.org/10.1016/j.jog.2014.09.004, 2015.

Beltrando, M., Lister, G.S., Forster, M., Dunlap, W.J., Fraser, G., and Hermann, J.: Dating microstructures by the $^{40}Ar/^{39}Ar$ step-heating technique: Deformation–pressure–temperature–time history of the Penninic Units of the Western Alps, Lithos, 113, 801–819, https://doi.org/10.1016/j.lithos.2009.07.006, 2009.

Bergemann, C.A., Gnos, E., and Whitehouse, M.J.: Insights into the tectonic history of the Western Alps through dating of fissure monazite in the Mont Blanc and Aiguilles Rouges Massifs, Tectonophysics, 750, 203–212, https://doi.org/10.1016/j.tecto.2018.11.013, 2019.

Bergemann, C.A., Gnos, E., Berger, A., Janots, E., and Whitehouse, M.J.: Dating tectonic activity in the Lepontine Dome and Rhone-Simplon Fault regions through hydrothermal monazite-(Ce), Solid Earth, 11, 199–222, https://doi.org/10.5194/se-11-199-2020, 2020.

Bertrand, A. and Sue, C.: Reconciling late faulting over the whole Alpine belt: from structural analysis to geochronological constrains, Swiss J. Geosci., 110, 565–580, https://doi.org/10.1007/s00015-017-0265-4, 2017.

549 Beucher, R., van der Beek, P., Braun, J., and Batt, G.E.: Exhumation and relief development in the
550   Pelvoux and Dora-Maira analysis and inversion of thermochronological age transects, J. Geophys.
551   Res., 117, F03030, https://doi.org/10.1029/2011JF002240, 2012.

552 Bons, P.D., Elburg, M.A., and Gomez-Rivas, E.: A review of the formation of tectonic veins and their
553   microstructures, J. Struct. Geol., 43, 33–62. https://doi.org/10.1016/j.jsg.2012.07.005, 2012.

554 Boutoux, A., Bellahsen, N., Nanni, U., Pik, R., Verlaguet, A., Rolland, Y., and Lacombe, O.: Thermal
555   and structural evolution of the external Western Alps: Insights from (U–Th–Sm)/He
556   thermochronology and RSCM thermometry in the Aiguilles Rouges/Mont Blanc massifs,
557   Tectonophysics, 683, 109–123, https://doi.org/10.1016/j.tecto.2016.06.010, 2016.

558 Cederbom, C.E., Sinclair, H.D., Schlunegger, F., and Rahn, M.K.: Climate induced rebound and
559   exhumation of European Alps, Geology, 32, 709–712, https://doi/10.1130/G20491.1, 2004.

560 Cenki-Tok, B., Darling, J.R., Rolland, Y., Dhuime, B., and Storey, C.D.: Direct dating of mid-crustal
561   shear zones with synkinematic allanite: new in situ U-Th-Pb geochronological approaches applied
562   to the Mont Blanc massif, Terra Nova, 26, 29–37, https://doi.org/10.1111/ter.12066, 2014.

563 Ceriani, S., Fügenschuh, B., and Schmid, S. M.: Multi-stage thrusting at the" Penninic Front" in the
564   Western Alps between Mont Blanc and Pelvoux massifs, Int. J. Earth Sci., 90(3), 685-702,
565   https://doi.org/10.1007/s005310000188, 2001.

566 Ceriani, S. and Schmid, S.M.: From N-S collision to WNW-directed post-collisional thrusting and
567   folding: Structural study of the Frontal Penninic Units in Savoie (Western Alps, France), Eclogae
568   geol. Helv., 97, 347–369, https://doi.org/10.1007/s00015-004-1129-2, 2004.

569 Champagnac, J. D., Molnar, P., Anderson, R. S., Sue, C., and Delacou, B.: Quaternary erosion-induced
570   isostatic rebound in the western Alps, Geology, 35(3), 195-198, https://doi/10.1130/G23053A.1,
571   2007.

572 Crespo-Blanc, A., Masson, H., Sharp, Z., and Cosca, M.: A stable and $^{40}Ar/^{39}Ar$ isotope study of a
573   major thrust in the Helvetic nappes (Swiss Alps): Evidence for fluid flow and constraints on nappe
574   kinematics, Geol. Soc. Am. Bull., 107(10), 1129-1144, https://doi.org/10.1130/0016-
575   7606(1995)107<1129:ASAAAI>2.3.CO;2, 1995.

576 Duchêne, S., Blichert-Toft, J., Luais, B., Télouk, P., Lardeaux, J.-M., and Albarède, F.: The Lu–Hf
577   dating of garnets and the ages of the Alpine high-pressure metamorphism, Nature, 387, 586–589,
578   https://doi.org/10.1038/42446, 1997.

579 Dumont, T., Schwartz, S., Guillot, S., Simon-Labric, T., Tricart, P., and Jourdan, S.: Structural and
580   sedimentary records of the Oligocene revolution in the Western Alpine arc, J. Geodyn., 56–57, 18–
581   38, https://doi.org/10.1016/j.jog.2011.11.006, 2012.

582 Goodfellow, B.W., Viola, G., Bingen, B., Nuriel, P., and Kylander-Clark, A.R.C.: Palaeocene faulting
583   in SE Sweden from U-Pb dating of slickenfibre calcite, Terra Nova, 29, 321–328,
584   https://doi.org/10.1111/ter.12280, 2017.

585 Janots, E., Grand'Homme, A., Bernet, M., Guillaume, D., Gnos, E., Boiron, M. C., Rossi, M.,
586   Seydoux-Guillaume, A.-M., and De Ascenção Guedes, R.: Geochronological and thermometric

evidence of unusually hot fluids in an Alpine fissure of Lauzière granite (Belledonne, Western Alps), Solid Earth, 10(1), 211-223, https://doi.org/10.5194/se-10-211-2019, 2019.

Jochum, K. P., Weis, U., Stoll, B., Kuzmin, D., Yang, Q., Raczek, I., Jacob, D.E., Stracke, A., Birbaum, K., Frick, D.A., Günther, D., and Enzweiler, J.: Determination of reference values for NIST SRM 610–617 glasses following ISO guidelines, Geostand. Geoanal. Res., 35(4), 397-429. https://doi/10.1111/j.1751-908X.2011.00120.x, 2011.

Kim, S.-T., Coplen, T.B., and Horita, J.: Normalization of stable isotope data for carbonate minerals: Implementation of IUPAC guidelines, Geochim. Cosmochim. Ac., 158, 276–289, https://doi.org/10.1016/j.gca.2015.02.011, 2015.

Lanari, P., Guillot, S., Schwartz, S., Vidal, O., Tricart, P., Riel, N., and Beyssac, O.: Diachronous evolution of the alpine continental wedge: evidences from P-T estimates in the Briançonnais Zone houillère (France-Western Alps), J. Geodyn., 56-57, 39–54, https://doi.org/10.1016/j.jog.2011.09.006, 2012.

Lanari, P., Rolland, Y., Schwartz, S., Vidal, O., Guillot, S., Tricart, P., and Dumont, T.: P-T-t estimation of syn-kinematic strain in low-grade rocks (<300°C) using thermodynamic modelling and $^{40}Ar/^{39}Ar$ dating techniques: example of the Plan-de-Phasy shear zone (Briançonnais Zone, Western Alps), Terra Nova, 26, 130–138, https://doi.org/10.1111/ter.12079, 2014.

Lardeaux J.M., Schwartz S., Tricart P., Paul A., Guillot S., Béthoux N., and Masson F.: A crustal-scale cross-section of the southwestern Alps combining geophysical and geological imagery, Terra Nova, 18 (6), 412-422, https://doi.org/10.1111/j.1365-3121.2006.00706.x, 2006.

Larroque, C., Delouis, B., Godel, B., and Nocquet, J.-M.: Active deformation at the southwestern Alps–Ligurian basin junction (France–Italy boundary): Evidence for recent change from compression to extension in the Argentera massif, Tectonophysics, 467, 22–34, https://doi.org/10.1016/j.tecto.2008.12.013, 2009.

Malusà, M., Zhao, L., Eva, E., Solarino, S., Paul, A., Guillot, S., Schwartz, S., Dumont, T., Aubert, C., Salimbeni, S., Pondrelli,S., Wang, and Q., Zhu, R.: Earthquakes in the western alpine mantle wedge, Gondwana Research, 44, 89-95, http://dx.doi.org/10.1016/j.gr.2016.11.012, 2017.

Mathey, M., Walpersdorf, A., Sue, C., Baize, S., and Deprez, A.: Seismogenic potential of the High Durance Fault constrained by 20 yr of GNSS measurements in the Western European Alps, Geophy. J. Int., 222(3), 2136-2146, https://doi.org/10.1093/gji/ggaa292, 2020.

Mugnier, J. L., Loubat, H., and Cannic, S.: Correlation of seismic images and geology at the boundary between internal and external domains of the Western Alps, Bull. Soc. Géol. Fr., 164(5), 697-708, 1993.

Nardini, N., Muñoz-López, D., Cruset, D., Cantarero, I., Martín-Martín, J., Benedicto, A., Gomez-Rivas, E., John, C., and Travé, A.: From Early Contraction to Post-Folding Fluid Evolution in the Frontal Part of the Bóixols Thrust Sheet (Southern Pyrenees) as Revealed by the Texture and Geochemistry of Calcite Cements, Minerals, 9, 117, https://doi.org/10.3390/min9020117, 2019.

Nocquet, J. M., Sue, C., Walpersdorf, A., Tran, T., Lenôtre, N., Vernant, P., Cushing, M., Jouanne, F., Masson, F., Baize, S., Chéry, J., and Van der Beek, P. A.: Present-day uplift of the western Alps, Sci. Rep., 6(1), 1-6, https://doi.org/10.1038/srep28404, 2016.

Passchier, C.W. and Trouw, R.A.J.: Microtectonics, 2nd rev. ed. Springer, Berlin, New York, 2005.

Paton, C., Hellstrom, J., Paul, B., Woodhead, J., and Hergt, J.: Iolite: Freeware for the visualisation and processing of mass spectrometric data, J. Anal. Atom. Spectrom., 26(12), 2508-2518, https://doi/10.1039/c1ja10172b, 2011.

Ring, U. and Gerdes, A.: Kinematics of the Alpenrhein-Bodensee graben system in the Central Alps: Oligocene/Miocene transtension due to formation of the Western Alps arc, Tectonics, 35(6), 1367-1391, https://doi.org/10.1002/2015TC004085, 2016.

Roberts, N.M.W., Rasbury, E.T., Parrish, R.R., Smith, C.J., Horstwood, M.S.A., and Condon, D.J.: A calcite reference material for LA-ICP-MS U-Pb geochronology: Calcite RM for LA-ICP-MS U-Pb dating, Geochem. Geophys. Geosyst., 18, 2807–2814, https://doi.org/10.1002/2016GC006784, 2017.

Roberts, N.M.W., Drost, K., Horstwood, M.S.A., Condon, D.J., Chew, D., Drake, H., Milodowski, A.E., McLean, N.M., Smye, A.J., Walker, R.J., Haslam, R., Hodson, K., Imber, J., and Beaudoin, N.: LA-ICP-MS U-Pb carbonate geochronology: strategies, progress, and application to fracture-fill calcite, Geochronology, https://doi.org/10.5194/gchron-2019-15, 2020.

Rolland, Y., Rossi, M., Cox, S. F., Corsini, M., Mancktelow, N., Pennacchioni, G., Fronari, M., and Boullier, A.M.: ^{40}Ar/^{39}Ar dating of synkinematic white mica: insights from fluid-rock reaction in low-grade shear zones (Mont Blanc Massif) and constraints on timing of deformation in the NW external Alps, Geological Society, London, Special Publications, 299(1), 293-315, https://doi.org/10.1144/SP299.18, 2008.

Rolland, Y. and Rossi, M.: Two-stage fluid flow and element transfers in shear zones during collision burial-exhumation cycle: Insights from the Mont Blanc Crystalline Massif (Western Alps), J. Geodyn., 101, 88-108, https://doi.org/10.1016/j.jog.2016.03.016, 2016.

Rossi, M., Rolland, Y., Vidal, O., and Cox, S.F.: Geochemical variations and element transfer during shear-zone development and related episyenites at middle crust depths: insights from the Mont Blanc granite (French-Italian Alps), Geological Society, London, Special Publications, 245, 373–396, https://doi.org/10.1144/GSL.SP.2005.245.01.18, 2005.

Rossi, M. and Rolland, Y.: Stable isotope and Ar/Ar evidence of prolonged multiscale fluid flow during exhumation of orogenic crust: Example from the Mont Blanc and Aar Massifs (NW Alps): Multi-scale fluid flow in the Alps, Tectonics, 33, 1681–1709, https://doi.org/10.1002/2013TC003438, 2014.

Rothé, E.: La seismicité des Alpes occidentales. Annales de l'Institut de Physique du Globe de Strasbourg, III, 1941.

Rubatto, D. and Hermann, J.: Zircon formation during fluid circulation in eclogites (Monviso, Western Alps): implications for Zr and Hf budget in subduction zones, Geochim. et Cosmochim. Ac., 67, 2173–2187, https://doi.org/10.1016/S0016-7037(02)01321-2, 2003.

Salimbeni, S., Zhao, L., Malusà, M., Guillot, S., Pondrelli, S., Margheriti, L., Paul, A., Solarino, S., Aubert, C., Dumont, T., Schwartz, S., Wang, Q., Xu, X., Zheng, T., and Zhu, R.: Fossil and active mantle flows in the western Alpine region unravelled by seismic anisotropy analysis and high-resolution P wave tomography, Tectonophysics, 731-732, 35–47, https://doi.org/10.1016/j.tecto.2018.03.002, 2018.

Sanchez, G., Rolland, Y., Schneider, J., Corsini, M., Oliot, E., Goncalves, P., Verati, C., Lardeaux, J.-M., and Marquer D.: Dating low-temperature deformation by $^{40}Ar/^{39}Ar$ on white mica, insights from the Argentera-Mercantour Massif (SW Alps), Lithos, 125(1-2), 521-536, https://doi.org/10.1016/j.lithos.2011.03.009, 2011.

Seward, D. and Mancktelow, N.S.: Neogene kinematics of the central and western Alps: Evidence from fission-track dating, Geology, 22(9), 803-806, https://doi.org/10.1130/0091-7613(1994)022<0803:NKOTCA>2.3.CO;2, 1994.

Schmid, S.M. and Kissling, E.: The arc of the western Alps in the light of geophysical data on deep crustal structure, Tectonics, 19, 62–85, https://doi.org/10.1029/1999TC900057, 2000.

Schwartz, S., Lardeaux, J.M., Tricart, P., Guillot, S., and Labrin, E.: Diachronous exhumation of HP-LT metamorphic rocks from south-western Alps: evidence from fission-track analysis, Terra Nova, 19, 133–140, https://doi.org/10.1111/j.1365-3121.2006.00728.x, 2007.

Schwartz, S., Gautheron, C., Audin, L., Dumont, T., Nomade, J., Barbarand, J., Pinna-Jamme, R., and van der Beek, P.: Foreland exhumation controlled by crustal thickening in the Western Alps, Geology, 45, 139-142, https://doi.org/10.1130/G38561.1, 2017.

Simon-Labric, T., Rolland, Y., Dumont, T., Heymes, T., Authemayou, C., Corsini, M., and Fornari, M.: $^{40}Ar/^{39}Ar$ dating of Penninic Front tectonic displacement (W Alps) during the Lower Oligocene (31-34 Ma), Terra Nova, 21, 127–136, https://doi.org/10.1111/j.1365-3121.2009.00865.x, 2009.

Smeraglia, L., Fabbri, O., Choulet, F., Buatier, M., Boulvais, P., Bernasconi, S.M., and Castorina, F.: Syntectonic fluid flow and deformation mechanisms within the frontal thrust of a foreland fold-and-thrust belt: Example from the Internal Jura, Eastern France, Tectonophysics, 778, 228178. https://doi.org/10.1016/j.tecto.2019.228178, 2020.

Sternai, P., Sue, C., Husson, L., Serpelloni, E., Becker, T.W., Willett, S.D., Faccenna, C., Di Giulio, A., Spada, G., Jolivet, L., Valla, P., Petit, C., Nocquet, J.-M., Walpersdorf, A., and Castelltort, S.: Present-day uplift of the European Alps: Evaluating mechanisms and models of their relative contributions, Earth-Sci. Rev., 190, 589–604, https://doi.org/10.1016/j.earscirev.2019.01.005, 2019.

Sue, C. and Tricart, P.: Late Alpine brittle extension above the Frontal Pennine Thrust near Briançon, Western Alps, Eclogae Geol. Helv., 92(2), 171-181, https://doi.org/10.5169/SEALS-168659, 1999.

Sue, C. and Tricart, P.: Neogene to ongoing normal faulting in the inner western Alps: a major evolution of the alpine tectonics, Tectonics, 22, 1–25, https://doi.org/10.1029/2002TC001426, 2003.

Sue, C., Delacou, B., Champagnac, J.-D., Allanic, C., Tricart, P., and Burkhard, M.: Extensional neotectonics around the bend of the Western/Central Alps: an overview, Int. J. Earth Sci. (Geol Rundsch), 96, 1101–1129, https://doi.org/10.1007/s00531-007-0181-3, 2007.

Sue, C., Thouvenot, F., Fréchet, J., and Tricart, P.: Widespread extension in the core of the western Alps revealed by earthquake analysis, J. Geophy. Res.-Sol. Ea., 104(B11), 25611-25622, https://doi.org/10.1029/1999JB900249, 1999.

Tardy, M., Deville, E., Fudral, S. E. R. E., Guellec, S., Ménard, G., Thouvenot, F., and Vialon, P.: Interprétation structurale des données du profil de sismique réflexion profonde ECORS-CROP Alpes entre le front Pennique et la ligne du Canavese (Alpes occidentales), Mém. S. Géo. F., 156, 217-226, 1990.

Thouvenot, F., Fréchet, J., Pinter, N., Gyula, G., Weber, J., Stein, S., and Medak, D. (Eds.): Seismicity along the northwestern edge of the Adria Microplate, The Adria Microplate: GPS Geodesy, Tectonics and Hazards, Nato Si. S. IV Ear. En. Kluwer Academic Publishers, Dordrecht, 335–349. https://doi.org/10.1007/1-4020-4235-3_23, 2006.

Tricart, P.: From passive margin to continental collision; a tectonic scenario for the Western Alps, Am. J. Sci., 284(2), 97-120, https://doi.org/10.2475/ajs.284.2.97, 1984.

Tricart, P., Schwartz, S., Sue, C., Poupeau, G., and Lardeaux, J.-M.: La denudation tectonique de la zone ultradauphinoise et l'inversion du front brianconnais au sud-est du Pelvoux (Alpes occidentales); une dynamique miocene a actuelle, B. Soc. Geol. Fr., 172(1), 49-58, https://doi.org/10.2113/172.1.49, 2001.

Tricart, P., Lardeaux, J.-M., Schwartz, S., and Sue, C.: The late extension in the inner western Alps: a synthesis along the south-Pelvoux transect, B. Soc. Geol. Fr., 177, 299–310, https://doi.org/10.2113/gssgfbull.177.6.299, 2006.

Tricart, P., Van Der Beek, P., Schwartz, S., and Labrin, E.: Diachronous late-stage exhumation across the western Alpine arc: constraints from apatite fission-track thermochronology between the Pelvoux and Dora-Maira Massifs, J. Geol. Soc., 164, 163–174, https://doi.org/10.1144/0016-76492005-174, 2007.

Vermeesch, P.: IsoplotR: A free and open toolbox for geochronology, Geosci. Front., 9(5), 1479-1493, https://doi.org/10.1016/j.gsf.2018.04.001, 2018.

Walker, J., Cliff, R.A., and Latham, A.G.: U-Pb isotopic age of the StW 573 hominid from Sterkfontein, South Africa. Science, 314(5805), 1592-1594, https://doi/10.1126/science.1132916, 2006.

Walpersdorf, A., Pinget, L., Vernant, P., Sue, C., Deprez, A., and the RENAG team.: Does Long-Term GPS in the Western Alps Finally Confirm Earthquake Mechanisms? , Tectonics, 37, 3721–3737. https://doi.org/10.1029/2018TC005054, 2018.

Wells, D. L., and Coppersmith, K. J.: New empirical relationships among magnitude, rupture length, rupture width, rupture area, and surface displacement, Bull. Seismol. Soc. Am., 84(4), 974-1002, 1994.

Woodhead, J.D. and Hergt, J.M.: Strontium, Neodymium and Lead Isotope Analyses of NIST Glass Certified Reference Materials: SRM 610, 612, 614, Geostand. Geoanal. Res., 25, 261–266, https://doi.org/10.1111/j.1751-908X.2001.tb00601.x, 2001.

740   Zhao, L., Paul A., Solarino S., Guillot S., Malusà M., Zheng T., Aubert C., Salimbeni S., Dumont T.,

741   Schwartz S., Pondrelli S., Zhu R., and Wang Q. First seismic evidence for continental subduction

742   beneath the Western Alps, Geology, 43, 815-818, https://doi.org/10.1130/G36833.1, 2015.